Chemical Engineering Journal 528 (2026) 172327

Contents lists available at ScienceDirect

Chemical Engineering Journal

journal homepage: www.elsevier.com/locate/cej

Electrocatalytic CO_2 reduction to produce efficient and controlled syngas on highly dispersed NiFe on N-doped ordered porous carbonaceous support

Ruben Palacio [a], Daniela Jaramillo [a], Elías Rodríguez-Jara [b,c], Ryosuke Nakazato [d], Matthias Quintelier [e], Keeko Matsumoto [d], Joke Hadermann [e], Kiyoharu Tadanaga [d], Nataly Carolina Rosero-Navarro [b,*]

[a] Grupo de Investigación Ciencia de los Materiales, Instituto de Química, Facultad de Ciencias Exactas y Naturales, Universidad de Antioquia UdeA, Calle 70 No 52-21, Medellín, Antioquia, 050010, Colombia
[b] Instituto de Cerámica y Vidrio, CSIC, Madrid, 28049, Spain
[c] Escuela de Doctorado UAM, Centro de Estudios de Posgrado, Universidad Autónoma de Madrid, C/ Francisco Tomás y Valiente, n° 2. Ciudad Universitaria de Cantoblanco, 28049, Madrid, Spain
[d] Faculty of Engineering, Hokkaido University, Sapporo, Hokkaido, 060–8628, Japan
[e] EMAT, Department of Physics, University of Antwerp, 2020, Antwerp, Belgium

ARTICLE INFO

Keywords:
Highly dispersed transition metals
Ordered porous carbonaceous materials
Electrochemical reduction of CO_2
Syngas ($CO + H_2$)
N-doped carbonaceous support

ABSTRACT

The electrocatalytic reduction of CO_2 to CO to produce syngas ($CO + H_2$) is of outmost scientific and technological significance to reduce the CO_2 concentration in the atmosphere and produce high-added valued chemicals. The atomic-level dispersion of Ni, Fe, and Zn species on an N-doped, ordered porous carbon support revealed that conductivity, Faradaic efficiency toward CO, and the CO/H_2 molar ratio are strongly influenced by the electrocatalyst's metal composition, the surface atomic ratios among the metals, and the textural and structural characteristics of the carbon support. The simultaneous dispersion of Ni and Fe resulted in a more efficient electrocatalyst than the monometallic Ni or the combination of Ni and Zn, in a high concentrated 1.0 M $KHCO_3$ electrolyte, relevant for industrial applications. In bimetallic Ni—Fe catalysts, the surface atomic ratio played a critical role in catalytic activity. Specifically, a higher Ni-to-Fe surface ratio of 0.69:0.24 in the Fe_3Ni_7NCMK-3 electrocatalyst resulted in Ni^{2+} surface enrichment across diverse chemical environments, including Ni^{2+} species with lower electronic density. At a potential of −1.2 V vs. RHE, this composition achieved a high FE_{CO} of 85 % and a low FE_{H_2} of 9 %, with a CO production rate of 6.85×10^{-1} μmol CO s^{-1} m^{-2} per surface Ni^{2+} site. Remarkably, even at a lower potential of −0.8 V vs. RHE, it maintained a high FE_{CO} of 70 %. Furthermore, the CO/H_2 molar ratio could be tuned from 2:1 at −0.6 V to 9:1 at −1.2 V vs. RHE.

1. Introduction

Global warming is one of the major threats for biodiversity, human health, social and economic development. For instance, there is an urgent need to develop sustainable processes based on abundant and renewable materials for obtaining energy, chemicals, food and materials with net zero emissions. Greenhouse gas emissions (GGE), especially CO_2 emissions originated from the extensive utilization of fossil fuels, are recognized as the main contributors to the climate change driven by the increase in the average global temperatures in recent post-industrial decades [1]. Therefore, the need to reduce CO_2 emissions is a global priority. The United Nations Climate Change Conference (COP28) has stablished a goal for accelerating the decrease of GGE by 2030 in order to achieve the Paris Agreement [2]. Conversely, according to the International EIA, in 2023 the energy-related CO_2 emissions reached a historic record high of 37.4 billion tonnes [3]. However, the high concentration of CO_2 offers a unique opportunity for storing renewable energy into chemical bonds, leading to the potential production of valuable chemicals and energetic products [2,4,5]. The electrocatalytic CO_2 reduction reaction (ECO_2RR) can effectively transform CO_2 into a set of valuable chemicals such as CH_3OH, HCOOH, CH_3CH_2OH, C_2H_4, CH_3CHO, C_3H_7OH, as well as energetic compounds such as CO and CH_4; this approach could effectively contribute to mitigate global warming while using a waste to obtain added-value products and renewable

* Corresponding author.
E-mail address: rosero@icv.csic.es (N.C. Rosero-Navarro).

https://doi.org/10.1016/j.cej.2025.172327
Received 22 June 2025; Received in revised form 21 November 2025; Accepted 25 December 2025
Available online 29 December 2025

energy [6,7].

Nevertheless, the ECO_2RR faces several challenges such as the stability of CO_2, the structure-sensitivity of the reaction, and the competition of the hydrogen evolution reaction (HER) [2]. Besides, the ECO_2RR is characterized by a set of multiple steps involving electron and proton exchange [8]. These challenges necessitate the development of highly active and selective catalysts to steer the reaction toward target products with high Faradaic efficiency (FE), low overpotential, and long-term stability.

The ECO_2RR can produce synthesis gas (syngas), $CO + H_2$, which can then be transformed into hydrocarbons through the Fischer-Tropsch reaction, or to alcohols such as CH_3OH [6,9–11], the molar ratio between CO/H_2 is crucial to determine the products that can be obtained [12], thus CO is considered one of the most valuable products in CO_2 electroreduction [13]. The ECO_2RR to CO proceeds through a two-proton/two-electron transfer in different complex reaction pathways [8,11,14]: 1. The first step is the CO_2 adsorption and activation to form the *COOH intermediate, which has to be strongly adsorbed to facilitate CO_2 activation, and in turn the reaction proceeds through two different steps: i) two steps throughout the adsorption and activation of CO_2 to $*CO_2^-$, mediated by the transfer of one electron, followed by the conversion of $*CO_2^-$ to *COOH, mediated by the transfer of one H^+ or ii) one step throughout the adsorption and activation of CO_2 to *COOH, mediated by the transfer of one electron and one H^+ [8]. 2. Then after, the *COOH intermediate is converted into *CO through a one-proton/one-electron transfer [11] with the release of one water molecule [8], the *CO must be weakly adsorbed to facilitate its desorption from the surface releasing the desired CO. The linearity and strength of the C═O bond in CO_2, the similar high binding energies of *COOH and *CO, and comparable thermodynamic redox potentials of multiple intermediates challenge selectivity and require high overpotentials to effectively transform CO_2 into CO, and importantly at high overpotentials the hydrogen evolution reaction (HER) becomes a major competitor reaction with CO_2 transformation [11,14]. For instance, the design of a multifunctional heterogeneous catalyst is of outmost importance for effectively activating CO_2 through *COOH and releasing CO, by efficiently allowing the 2-proton/2-electron transfer during the reaction. The fine tailoring of heterointerfaces plays a crucial role in obtaining highly active and stable electrocatalysts as in the case of oxygen evolution reaction (OER) [15], and electrochemical oxidation of methane [16]. Ag–Cu–NC hierarchical electrocatalysts produces CO on an Ag layer during ECO_2RR, which is then transferred to a Cu/NC interface enhancing *CO trapping and adsorption, favoring C_2H_4 formation with a FE of 53.5 % [17].

In recent years, single atom catalysts (SACs) are widely investigated by the catalytic community because several metals have demonstrated activity in the electrocatalytic CO_2 reduction to CO [2,10,14,18–20]. SACs maximize atomic efficiency and exhibit high selectivity in a wide number of catalytic reactions [21]. The challenge is a precise synthesis of the materials with high stability and the understanding of the physical and chemical properties responsible for their intrinsic activity. Transition metal complexes, with N-containing organic ligands, can effectively stabilize metal cations leading to the preparation of N-doped carbonaceous materials and highly dispersed multimetallic active sites [22]. In addition, N-functional groups generate surface defects which can promote catalytic activity [2,11,23–25]. For instance, atomically dispersed transition metals in an N-doped carbonaceous material M-N-C, with M = Fe, Co, Ni, Cu, were evaluated in the ECO_2RR [19], M-N-C are considered as promising electrocatalytic materials for ECO_2RR [8]. In the case of Ni as active phase, the results evidenced that Ni, Ni-N-C, was the most active electrocatalyst with a *FE* for CO of 97 % at −0.65 V vs. RHE. Experimental and theoretical analysis showed that Ni^{2+} species with d-vacant orbitals favored electron transfer from C in CO_2 molecules, thus enhancing adsorption and activation of CO_2. It has been reported that with Ni—N— and Fe-N-containing materials in M-N_4 structures, high electron conductivity and strong bonding between *COOH intermediates and metal centers are achieved, for instance decreasing the overall reaction barriers and promoting CO selectivity [26].

In other work, single Ni sites dispersed on a N-doped carbon (Ni SAs/N-C) were prepared by calcination of Ni-MOF, obtaining highly dispersed Ni-N_3C_1 species as the active sites [27]. This catalyst exhibited a *FE* for CO of 71.9 % at −0.89 V vs. RHE, and current density of 10.48 mA cm^{-2}. Furthermore, Ni dispersed as single atoms in an N-doped graphene support was obtained by pyrolysis in Ar of a mixture of L-alanine (A-Ni-NG) or L-cysteine as S precursor (A-Ni-NSNG), melamine and nickel acetate [28]. The presence of S resulted in a material with richer surface defects. The A-Ni-NSNG showed a FE_{CO} of ~97 % at −0.5 V vs. RHE, without production of CH_4 because of the low binding energy of CO on atomically dispersed Ni active sites, besides the activity of the catalysts was maintained for over 100 h, keeping 98 % of the initial current for CO formation. The main active species was Ni(I), and characterization before and after electrocatalytic measurements using XPS demonstrated high stability under reaction conditions [28]. Ni- and N-codoped carbon materials showed high *FE* in CO_2 selective reduction to CO [29]. Ni, N-codoped hollow carbon particles were obtained from a mixture of tannin, nickel acetate and melamine by ball milling and further carbonization at temperatures between 700 and 900 °C. The resulting porous materials showed highly dispersed Ni nanoparticles embedded in the N—C carbon matrix and high surface area. The electrocatalytic activity in ECO_2RR depended on the carbonization temperature and Ni loading which, particularly affected the speciation of N. The electrocatalyst obtained after carbonization at 800 °C, 2 mM-Ni,N-C-800, showed a Electrochemical Surface Area (ESCA, C_{dl}) of 3.5 mF cm^{-2} with a *FE* for CO of 94.8 % at −0.86 V vs. RHE, and current density of 18.2 mA cm^{-2} [29]. The authors reported that the ratio Ni—N and the presence of pyridinic-N species were at the origin of the high performance of the 2 mM-Ni,N-C-800 electrocatalyst with regard to other materials. Ni embedded in N-doped carbon nanotube (Ni@NCNT-C) also showed high activity in ECO_2RR to CO, the textural properties and activity were dependent on Ni content and carbonization temperature [30]. The Ni@NCNT-C materials were obtained from carbonization of a crystalline porous material, zeolitic imidazolate framework (ZIF-8), with high carbon content and large surface area. The best electrocatalyst was 0.1 Ni@NCNT-C-800 i.e., obtained with a mol ratio Ni/ZIF-8 of 0.1 and carbonization at 800 °C, showing a *FE* to CO of ~90 % at −0.77 V vs. RHE, with current density of 28 mA cm^{-2} at −1.17 V vs. RHE, and the activity was maintained for over 40 h. XPS analysis performed before and after the reaction allowed the authors to conclude that adsorption of CO_2 on pyridinic-N led to form pyridonic N, and that the ECO_2RR takes place on the pyridinic-N active sites. In addition, Ni-containing materials exhibited better ECO_2RR catalytic performance than Mn-, Fe-, Co-, and Cu-containing metals [30]. Nevertheless, the Ni—N catalysts are limited by the slow kinetics of CO_2 to *COOH and weak *H adsorption [26]. For instance, despite the potential of Ni-based catalysts in ECO_2RR to CO, multimetallic catalysts have also been studied, this strategy leads to more active electrocatalysts [9], improving the adsorption and activation properties of CO_2, selectivity and stability.

Bimetallic Fe—Ni nanoparticles embedded in a N-doped carbonaceous material, with a graphene-like lamellae structure, were obtained from the carbonization of a dried suspension of $FeCl_3{\cdot}6H_2O$/$NiCl_2{\cdot}6H_2O$/dicyandiamine/glucose [31]. The bimetallic materials showed the formation of an $Fe_{0.64}Ni_{0.36}$ alloy, and an average particle size of FeNi of 9 nm. The best performance in the ECO_2RR reaction was obtained with a Fe_2Ni/NG catalyst exhibiting a FE_{CO} of 60.9 % at −0.6 V vs RHE, with a current density of 3.40 mA cm^{-2} [31]. The syngas produced was obtained with a CO/H_2 ratio between 1.2 and 2.9, and the activity was maintained for over 12 h. The electrocatalytic performance of the materials was attributed to the Fe—Ni alloy embedded in the C shells, with N doping enhancing charge transfer and catalyst stability under reaction conditions. Additionally, the formation of active sites related to pyridine-N, Fe—N, and pyrrole-N species contributed to the

improved performance. In another study, bimetallic Fe—Ni supported on a N-doped carbonaceous support, FeNi-NC, obtained from carbonization of a FeNi-ZIF with different molar ratios of Ni/Fe as simultaneous precursor for Fe, Ni, N, C, O, was evaluated in the ECO_2RR to produce controlled syngas [23]. The most active catalyst, Fe_3Ni_7-NC obtained after carbonization at 800 °C, showed a FE_{CO} of 81.3 % at −0.9 V vs. RHE, FE_{H_2} of 41 % at −0.5 V vs RHE, with adjusted CO/H_2 ratio between 1:1–6:1 in a wide potential range. The materials showed the formation of $FeNi_3$ clusters embedded in the carbonaceous matrix. The electrocatalytic performance of Fe_3Ni_7-NC carbonized at 800 °C, compared to monometallic catalysts, other carbonization temperatures, and Ni/Fe ratios, was attributed to the presence of both metals in the dual catalyst, which enhanced the charge transfer rate, current density, and electrochemically active area, as well as the increased Ni—N content.

In this work, phenanthroline complexes of transition metals (Fe, Ni, Zn) were used as precursors for C, N, and transition metals with the aim of obtaining highly dispersed multimetallic species confined in an N-doped ordered porous carbonaceous support, as efficient electrocatalysts in the selective electrocatalytic reduction of CO_2 to syngas ($CO + H_2$), which is seen as a high energy value product for sustainable energy development and C1 chemistry [32]. Additionally, syngas can be used in internal combustion engines as a substitute for petroleum fuels [33].

2. Experimental

2.1. Synthesis of materials

Porous carbonaceous materials containing N, and mono- or bimetallic Fe, Ni, Co, Zn were synthesised through the nanocasting methodology using phenanthroline complexes as precursor for C, N, and metals; and SBA-15 silica as hard-template [34].

2.1.1. SBA-15 preparation

12 g of P123 surfactant was dissolved in aqueous HCl solution containing 37 g of HCl (37 %) and 360 g of ultrapure water, at 35 °C under magnetic stirring, followed by the addition of 24 g of tetra ethyl ortho silicate (TEOS), and the resulting mixture was kept for 24 h under magnetic stirring at 35 °C [35]. Afterward, the suspension was hydrothermally treated at 140 °C for 24 h. Then, the powder was recovered by filtration without washing and air-dried at 80 °C. Finally, the silica powder was calcined in air at 550 °C for 3 h at a heating rate of 1 °C min^{-1}.

2.1.2. Porous carbonaceous materials preparation

Phenanthroline (Phe) coordination compounds were prepared with a molar ratio Phe: metal of 3: 1. The pore structure of the SBA-15 silica was subsequently impregnated with the aqueous phenanthroline coordination compounds solution. For instance, 2 different solutions were prepared: i) ***solution 1*** Phe was dissolved in ultrapure water acidified with H_2SO_4; ii) ***solution 2*** the nickel precursor, $Ni(NO_3)_3{\cdot}6H_2O$, was dissolved in ultrapure water. Then, solution 2 was slowly added to solution 1 to obtain the corresponding coordination compound (solution 3). Then after, a volume of solution 3, equal to the pore volume corresponding to the amount of the SBA-15 template, was added dropwise to the SBA-15 silica with mechanical stirring. The resulting powder was dried at 80 °C, then carbonized at 800 °C for 3 h (heating rate: 5 °C min^{-1}) under N_2 atmosphere. Finally, the SBA-15 template was dissolved with a NaOH aqueous solution (5 wt%). The carbonaceous material was recovered by centrifugation, washed with ultrapure water until neutral pH and dried at 100 °C. Following this procedure, in total 5 materials were obtained and named as follow: MNCMK-3 where M represents the metal (Ni) or the mixture of metals (FeNi, NiZn), N indicates that the materials contain N, CMK-3 indicates a carbonaceous material obtained by nanocasting of a SBA-15 silica hard-template. For the preparation of bimetallic samples i.e. containing two metals, the Phe: total metal molar ratio for the coordination compound solution was maintained at 3: 1 but the ratio between both metals was varied at 7/3 and 3/7, corresponding to a metal loading of 7 wt% and 3 wt%. The synthesised samples were named according to the ratio between both metals: Fe_3Ni_7NCMK-3, Fe_7Ni_3NCMK-3, Ni_3Zn_7NCMK-3.

2.2. Physicochemical characterization

Nitrogen adsorption and desorption isotherms were obtained by using a Brunauer–Emmett–Teller (BET) method. The samples were treated at 80 °C for 1 h and then degassed at 250 °C for 12 h. The crystalline structure of the materials was determined by X-ray diffraction (XRD), using a Malvern-PANalytical Modelo Empyrean 2012, equipped with a Pixel 3D detector, under Cu K_α radiation (1.541874 Å), operated at 45 kV and 40 mA; Goniometer: Omega/2theta, platform: Spinner rotating at 4 rpm. Scans were recorded at high angles, 2θ between 10° - 90°, the step was 0.05° with a time per step of 50 s; at low angles, 2θ between 0.5° - 5.0°, the step was 0.01° with a time per step of 70 s. The diffractograms were analysed with the HighScore Plus software.

Morphology and the distribution of the metals in the carbon matrix at micrometric level were studied by scanning electron microscopy (SEM) using a JEOL JSM-6490LV microscope with a LaB_6 filament operating at 20 kV accelerating voltage, equipped with an energy dispersive spectroscopy (EDX) detector for element mapping. SEM images were also recorded using a field emission scanning electron microscope (*ThermoFisher Quanta FEG 250 microscope)*. Scanning transmission electron microscopy energy dispersive X-ray analysis (STEM-EDX) analysis was performed on a *ThermoFisher Osiris microscope* operated at 200 kV and equipped with a *Super X-detector* system. Elemental maps were acquired with a minimum duration of 15 min to ensure sufficient count statistics. In order to study the morphology and distribution of the material with as limited effect as possible of the sample preparation, no ultrasonic bath was used during the procedure. The sample powder was dissolved in ethanol and then manually shaken to dissolve the particles further. After this, the solution was dropcasted on a TEM grid. Further analysis on morphology, pore structure, metals localization at nanometric scale was performed using High-Resolution Transmission Electron Microscopy (HRTEM) imaging on an image corrected *ThermoFisher Titan microscope* operated at 300 kV and equipped with a Gatan US1000 CCD camera.

X-Ray Photoelectron Spectroscopy (XPS) was performed on a *FlexPS-ARPES-E* (*SPECs*), with a microfocus source using a monochromatic Al-K_α of 1486.68 eV, operating at a voltage of 15 kV and a current of 6.6 mA. The high-resolution spectra were recorded using a pass energy of 30 eV with steps of 0.2 eV. The binding energy (BE) scale was calibrated by adjusting the adventitious carbon C—H to 284.8 eV. The XPS spectra were analysed using CasaXPS software, with an Off Shirley background and asymmetric functions were considered with a line shape SGL(*p*)T(k). The values of the Relative Sensitivity Factors (RSF), obtained from the Scofield database, were C 1s (1.0), N 1s (1.8), O 1s (2.93), Fe 2p (16.42), and Ni 2p (22.18). Signals 1s have the same FWHM. Signals 2p, with spin-orbit coupling $2p_{3/2}$ and $2p_{1/2}$, all peaks have the same FWHM. Additionally, the area of peaks associated with signals $2p_{1/2}$ being 0.5 of that of peaks associated with $2p_{3/2}$ signals.

2.3. Electronic conductivity measurements

Electronic conductivity measurements were performed following a reported procedure [36]. 11 mg of powdered sample of each compound is embedded at a pressure of 350 MPa for 5 min in a 6 mm diameter potshell with electrical connections to a potentiostat (SP-200, Biologic). Chronoamperometry measurements are made at −40, −20, −10, 0, 10, 20, 40 mV vs. E_{oc} allowing a 30 min stabilisation time for the assay before taking the current and potential value. A linear fit is carried out with the measurements taken for each compound, where the current is

represented on the ordinate axis and the potential on the abscissa axis. The electrical resistance of the compound can be obtained as the slope of the linear fit, according to Ohm's law (1) and the electronic conductivity can be calculated (2):

$$I = V \times R \quad (1)$$

$$\sigma = L/(R \times A) \quad (2)$$

Where I is the current intensity (A), V is the voltage (V), R is the electrical resistance. (Ω), σ is the electronic conductivity (S/m), L the thickness of the pellet (m) and A the cross-sectional area of the pellet (m^2).

2.4. Electrocatalytic characterization

Electrochemical study was performed in a three-compartments cell with a gas diffusion electrode (GDE) as working electrode (WE), to determine the electrocatalytic behaviour of the samples in Gas-phase CO_2RR, following a reported procedure [37]. The sample-loaded GDE was prepared by simple drop-casting of a catalyst ink consisted of 1 mg of synthesised samples, 30 μL of the binder (5 wt% Anion exchange resin in propanol solution), and 570 μL of ethanol as solvent mixed by grinding. This ink was deposited onto a carbon paper with gas-diffusion layer (GDL-36BB) with a coating circular-shape area of 1.55 cm^2 of diameter and later casted and dried at 100 °C. Briefly, a three-electrode setup was used, in which the sample-loaded carbon paper, a platinum wire electrode (*CE-100 A*, EC FRONTIER Co., Ltd.), and Ag/AgCl electrode (3.0 M KCl, *BAS Inc.*) were used as working, counter, and reference electrodes, respectively. The cathodic and anodic compartments were separated by an anion exchange membrane (AEM) to avoid the unexpected influence of the oxidation reaction taking place on the counter electrode. A CO_2-saturated 1 M aqueous $KHCO_3$ solution was used as the electrolyte. The CO_2 gas flowed with 50 mL/min flow rate to the cathodic compartment, and the catholyte solution was stirred at 600 rpm. Under the above conditions, CO_2 electroreduction for 30 min was performed by applying a range of voltage with an electrochemical analyser *(SP-200,* Biologic). Gas-phase products were detected by gas chromatography techniques (*GC-2014,* Shimadzu Corp.; carrier gas: nitrogen, flow rate: 10 mL/min, pressure: 53.2 kPa, vaporization chamber temperature: 120 °C) by collecting gas for in sample bags. For the detection of hydrogen (H_2), *Molecular Sieve 5 A* (GL Sciences Inc.; column temperature: 50 °C, injected sample volume: 1 mL) and a thermal conductivity detector (*TCD,* Shimadzu Corp.; detector temperature: 120 °C) were used. For the detection of CO, *PoraPak N* (GL Sciences Inc.; column temperature: 50 °C, injected sample volume: 1 mL) a flame ionization detector (*FID,* Shimadzu Corp.; detector temperature: 120 °C) was used.

The evaluation of the catalytic activity of CO_2RR was carried out through a potentiostatic measurement, where the current density was determined by applying point voltage values between −0.6 V and − 1.2 V against the reference hydrogen electrode (RHE). The electrode potentials in the study are converted to the reversible hydrogen electrode (E_{RHE}) or the standard hydrogen electrode (E_{SHE}) according to the following equations:

$$E_{RHE} = E_{SHE} + 0.059 \times pH \quad (3)$$

$$E_{SHE} = E_{Ag/AgCl} + 0.222 \quad (4)$$

Simultaneously, the gaseous products of the reaction were collected for 5 min by applying the specific potential. From the gas chromatographic analysis, the faradaic efficiency (*FE*) of the system in the evolution of CO and H_2, calculated from the expression (5) [38].

$$FE = (2VprF)/(IRT) \quad (5)$$

Where *V* is the volumetric concentration of CO or H_2 in the gas produced by the cell during the reaction. *I (*in *mA)* is the average current during the reaction, and *r* is the CO_2 flow rate ($m^3\ s^{-1}$) at room temperature and pressure. For the other constants in the formula, *p* is 1.013 × 105 Pa, *F* is 96,485C mol^{-1}, *R* is 8.3145 *J* mol^{-1} K^{-1}, and *T* is 298 K. All potentials and voltages in this work were evaluated without *iR* compensation.

The rate of CO produced was calculated according to expression (6):

$$r_{CO} = (\mu mol\ CO\ s^{-1}\ m^{-2})/(\text{surface atomic concentration of } Ni^{2+}) \quad (6)$$

where m^{-2} indicates the BET surface area of the catalyst at the electrode and the surface atomic concentration of Ni^{2+} was determined by XPS.

3. Results and discussion

3.1. Physicochemical characterization

3.1.1. Textural properties

N_2 adsorption-desorption isotherms are presented in Fig. 1. The materials exhibit a type-IV isotherm characteristic of mesoporous materials [39], but the isotherms also exhibit an increase in N_2-adsorption at low P/P_o (< 0.1) indicating the presence of micropores. Furthermore, the materials exhibit interparticle porosity due to the increase of N_2-adsorption at high P/P_o (> 0.85). The surface area and pore volume depend on the composition of materials, bimetallic materials having larger surface area and pore volume with regard to the monometallic material (Table 1). The materials NiNCMK-3 and Fe_3Ni_7NCMK-3 exhibit narrow pore size distributions (Fig. 1), while Fe_7Ni_3NCMK-3 shows a bimodal distribution. In contrast, Ni_3Zn_7NCMK-3 displays a broad pore size distribution with multiple maxima, indicating a more heterogeneous porous structure, likely due to unsuccessful nanoreplication at the mesopore level.

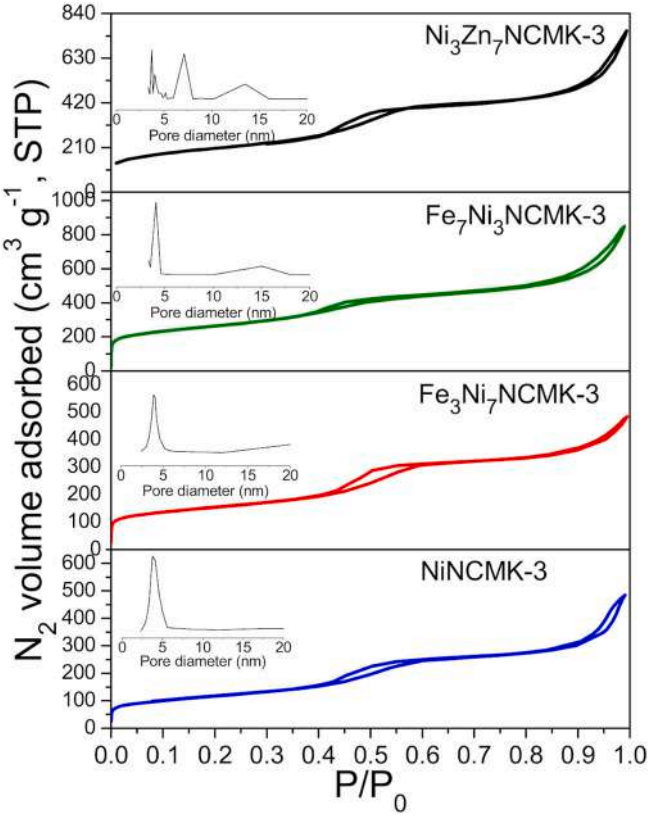

Fig. 1. N_2 adsorption-desorption isotherms and pore size distribution.

Table 1
Textural properties determined by N_2 adsorption-desorption. V_p was measured at $P/P_0 = 0.84$.

Sample	S_{BET} ($m^2\ g^{-1}$)	V_p ($cm^3\ g^{-1}$)
NiNCMK-3	410	0.44
Fe_3Ni_7NCMK-3	530	0.53
Fe_7Ni_3NCMK-3	897	0.80
Ni_3Zn_7NCMK-3	730	0.68

3.1.2. Structural and morphological properties

XRD patterns of synthesised materials are shown in Fig. 2. Low-angle diffraction patterns show several diffraction peaks for Fe_3Ni_7NCMK-3, and Ni_3Zn_7NCMK-3 indicating an ordered porous structure (Fig. 2a), while the monometallic material containing only nickel and the powder prepared with a higher molar ratio of iron than nickel, NiNCMK-3 and Fe_7Ni_3NCMK-3 respectively, show only one diffraction peak suggesting a less ordered porous structure. These results signal that the porous structure depended on the composition of the phenanthroline complex i.e. the nature of the metals and their molar ratio. In the wide-angle diffraction patterns (Fig. 2b), two low-intensity and broad reflections are observed, corresponding to reflections from the graphitic framework. No characteristic peaks for metallic or metal oxide phases were identified in any of the materials analysed (Fig. 2b), indicating the absence of metallic or metal oxide nanoparticles and suggesting a high dispersion of the metal species in the powders.

The morphology and metal distribution at micrometric scale are analysed by SEM (Fig. 3) and EDX (Fig. 4). In all materials, the morphology of the SBA-15 silica template was successfully replicated, forming aggregates of rope-like particles [34], indicating successful micrometric-scale replication regardless of the metals used. Fig. 4 shows the results of STEM-EDX analysis. The elemental maps show a uniform distribution of metals within the carbon matrix, evidencing the potential of the phenanthroline complexes to produce highly dispersed metal species, likely reaching SACs distribution on carbonaceous CMK-3 materials. Additionally, the presence of nitrogen and sulfur (S) is also evidenced, the occurrence of S is attributed to the use of H_2SO_4 for the dissolution of phenanthroline. The mean atomic ratio between metals varied in function of the nature of the metals: i) Fe_3Ni_7NCMK-3 with a Fe:Ni of 0.43, comparable to the nominal value of 0.45, indicating that the amount of Ni is more than twice the amount of Fe as expected with regard to the preparation of the material; ii) Fe_7Ni_3NCMK-3 with a Fe:Ni ratio of 0.95 being lower than the nominal value of 2.45; iii) Ni_3Zn_7NCMK-3 with a Zn:Ni ratio of 1.25 being lower than the nominal value of 2.09.

Further analysis of the pore structure and nanoscale metal localization was carried out using HRTEM (Fig. 5). Despite the low resolution of XRD patterns at low angles, all materials displayed a well-defined and regular pore structure resembling the hexagonal ordering of the SBA-15 template. This indicates successful replication of the SBA-15 hard template in the metal-containing carbonaceous materials, regardless of the metal composition, whether monometallic or bimetallic, and independent of the metal loading. In all samples, a few clusters were observed that are not detectable by XRD, indicating that to some extent, the metals may aggregate into amorphous clusters (Fig. 5 and Fig. S1). This is particularly evident in the Fe_3Ni_7NCMK-3 catalyst, which shows larger aggregates. Nevertheless, STEM-EDX (Fig. 4) maps confirm a high degree of metal dispersion across all catalysts. Furthermore, the scarcity of visible clusters in HRTEM (Fig. 5) versus the homogeneous distribution of all elements on the EDX maps (Fig. 4) supports the proposition that the metals are dispersed mainly as single atoms.

3.1.3. Surface chemistry

The surface chemistry of materials was characterized by XPS (Fig. 6, Table 2). The survey spectra showed the presence of C, O, N and S in all catalysts (Table 2). The surface content of S is lower for samples containing Fe, in particular for the Fe_3Ni_7NCMK-3 material which showed higher nickel than iron surface atomic concentration. In the case of N, the results show comparable surface concentration of N in all materials with an average of 7.08 ± 0.64 at.%. The atomic surface concentration of Ni is higher in the case of the monometallic material, NiNCMK-3, and is lower in the bimetallic materials (Table 2). The surface concentration of Fe is lower than the concentration of Ni in both, Fe_3Ni_7NCMK-3 and Fe_7Ni_3NCMK-3 materials. The surface ratio between Fe and Ni, Fe:Ni, is lower in the Fe_3Ni_7NCMK-3 material with the surface atomic concentration of Ni being ~3 times the surface atomic concentration of Fe (Table 2), in agreement with STEM-EDX characterization.

The high-resolution N 1s spectra show 4 signals in all materials (Fig. 5a), indicating the presence of pyridinic-N, pyrrolic-N, graphitic-N, and pyridine-N-oxide species [40–42]; besides the bimetallic samples show an additional signal at higher binding energy demonstrating a more heterogeneous N speciation in these samples. The signal at 399.70

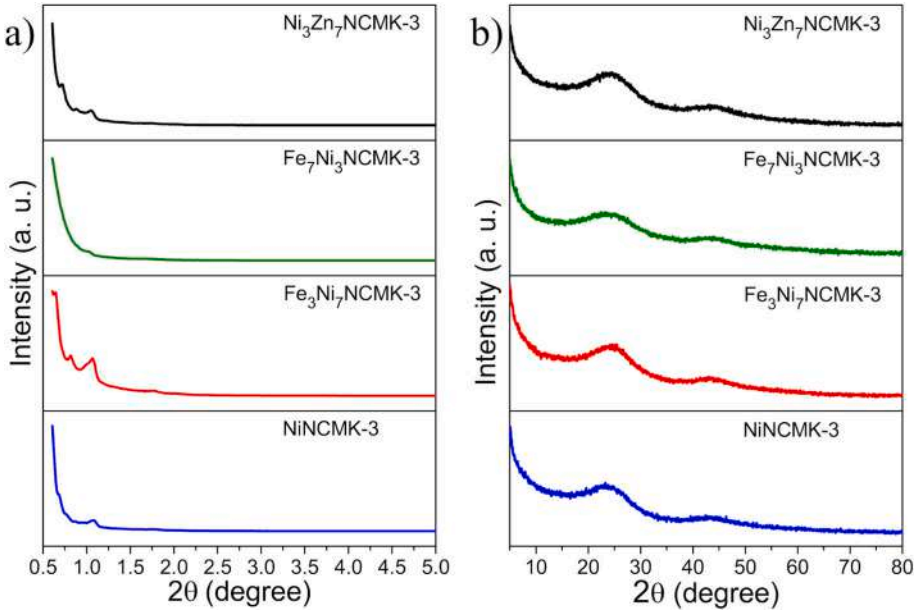

Fig. 2. XRD patterns of synthesised samples: a) Low angle, and b) large angle.

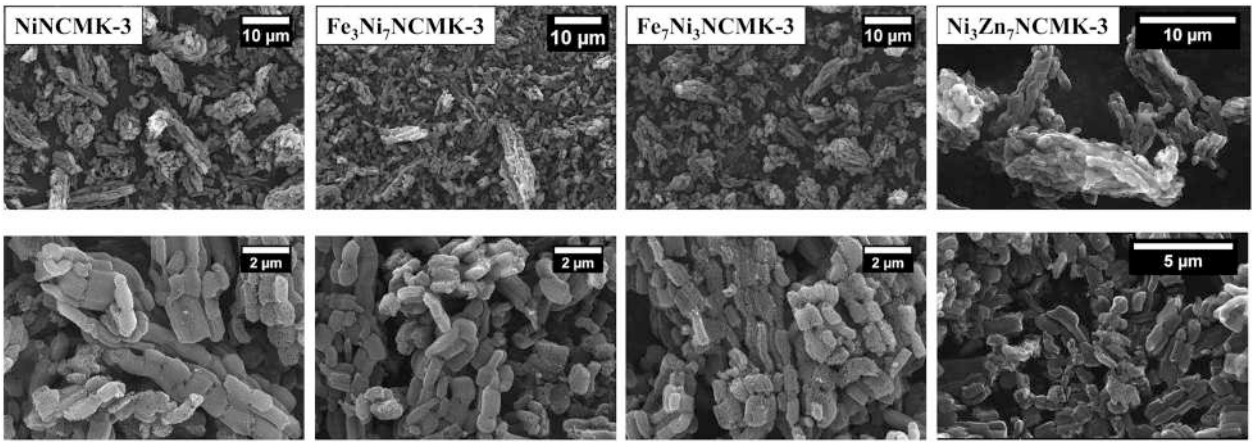

Fig. 3. SEM images of NiNCMK-3, Fe_3Ni_7NCMK-3, Fe_7Ni_3NCMK-3, and Ni_3Zn_7NCMK-3 powders.

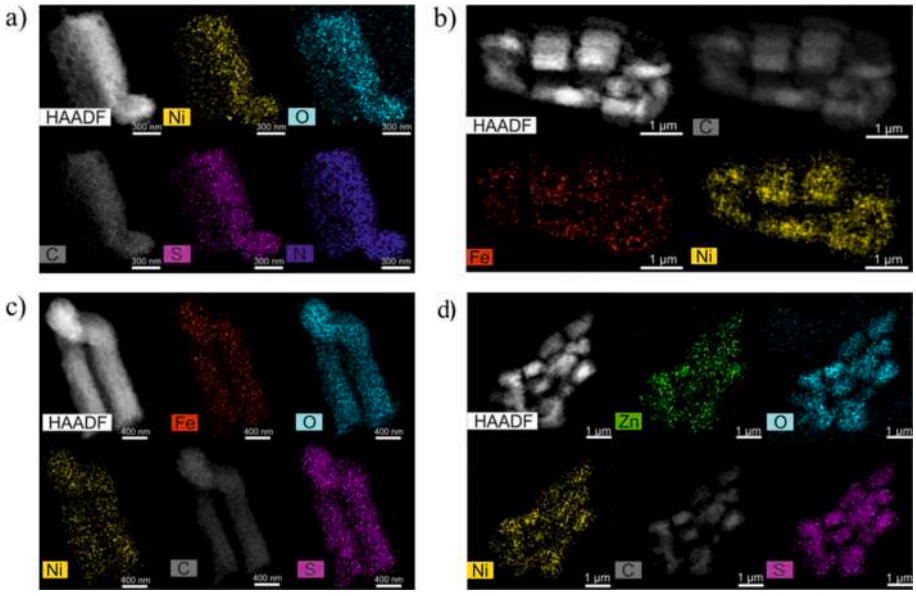

Fig. 4. STEM-EDX images for: a) NiNCMK-3, b) Fe_3Ni_7NCMK-3, c) Fe_7Ni_3NCMK-3, and d) Ni_3Zn_7NCMK-3. All maps are given in counts.

± 0.23 eV indicates the formation of metal-N bonds, Ni—N and Ni—Fe [19,23,31]. The main N species in all materials is pyridinic-N, followed by pyrrolic-N, both species considered as active sites for CO_2 reduction. The N 1s spectrum of Fe_3Ni_7NCMK-3 material also exhibits higher surface concentration of pyridine-N-oxide species and higher concentration of the species at 405.52 ± 0.55 eV, suggesting a more defect surface enrichment.

The high-resolution spectrum for Ni 2p exhibits the characteristic Ni $2p_{3/2}$ and Ni $2p_{1/2}$ doublet from the spin-orbit coupling (Fig. 5b), each photopeak shows the corresponding shake-up satellite structure at a higher binding energy. All spectra show a signal at 855.46 ± 0.16 eV characteristic of Ni^{2+} [43,44], which is the major species of nickel in the catalysts (Table 3). This signal can also indicate the formation of Ni—N bonds [23,30,31], in agreement with N 1s spectra. The spectrum of the Fe_7Ni_3NCMK-3 material shows a signal at 854.08 eV, indicating Ni^{2+} species in a different chemical environment perhaps created by the high loading of iron forming aggregates as observed by HRTEM (Fig. 5), donating electronic density to the system. The spectra of NiNCMK-3, Fe_3Ni_7NCMK-3 and Fe_7Ni_3NCMK-3 display a signal at 857.90 ± 0.38 eV indicating the formation of Ni^{3+} [43–45]. In contrast, Ni^{2+} is the only Ni species observed in the Ni_3Zn_7NCMK-3 material, while samples containing iron showed Ni^{2+} and Ni^{3+}, indicating a richer chemical environment, especially for Fe_3Ni_7NCMK-3. This material shows an additional signal at 856.14 eV for Ni^{2+} in a different chemical environment with lower electronic density, this species must be also generated by the presence of iron at an optimum Fe:Ni surface atomic ratio of 0.35 (Table 3). Therefore, the presence of iron modified the chemical environment and electronic density of Ni^{2+} species. For instance, Ni^{2+} species are the major species on the surface of Fe_3Ni_7NCMK-3 material, and this material also shows the higher total surface concentration of Ni^{2+} on the surface reaching 87.9 at.%.

The spectra of Fe in the 2p region, were of low intensity and low resolution. The spectrum of Fe_3Ni_7NCMK-3 was not processed, but the spectrum of Fe_7Ni_3NCMK-3 shows the characteristic Fe 2p doublet of the spin-orbit coupling. The signal at 710.90 eV can be attributed to the presence of Fe^{3+} species (Fig. 5c). The spectrum of Zn in the region 2p, Ni_3Zn_7NCMK-3 material, shows the characteristic doublet for $2p_{3/2}$ and $2p_{1/2}$ (Fig. 5d), indicating the formation of Zn^{2+} species [46].

3.2. Electronic conductivity

Calculated electronic conductivity results are shown in Table 4 for the different synthesised materials. The conductivity varies with the composition of the materials, the bimetallic materials showing higher

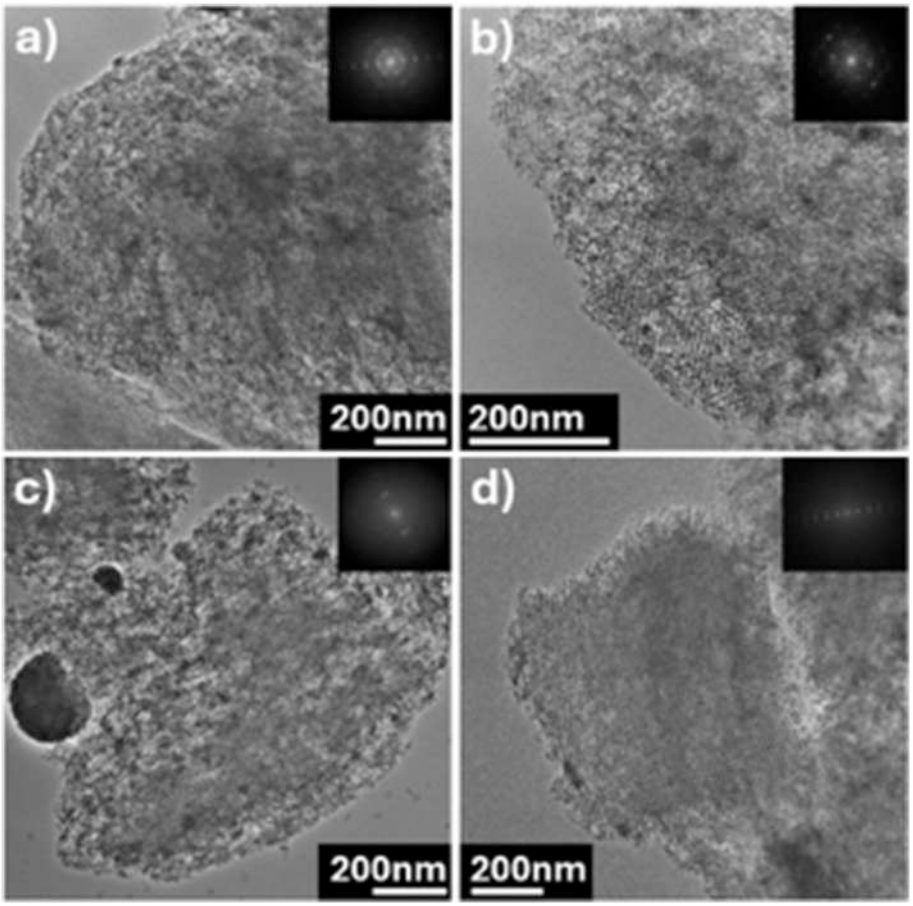

Fig. 5. HRTEM images of a) NiNCMK-3, b) Fe_3Ni_7NCMK-3, c) Fe_7Ni_3NCMK-3 and d) Ni_3Zn_7NCMK-3. The insets in the figures are the FFTs taken of the respective image.

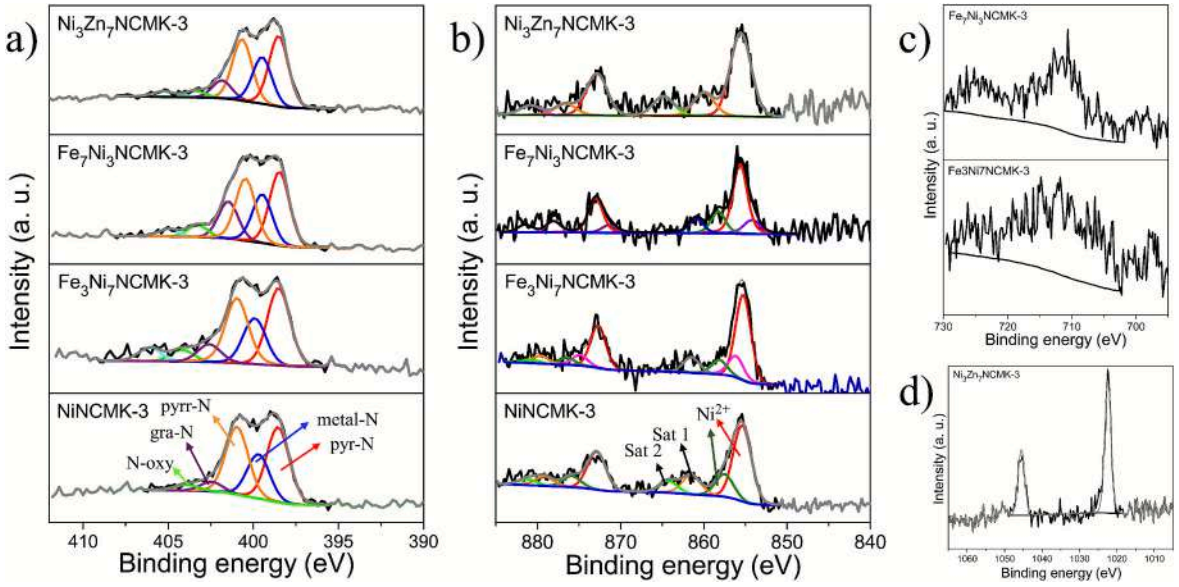

Fig. 6. XPS spectra for: a) N 1 s, b) Ni 2p, c) Fe 2p, and d) Zn 2p.

conductivity than the monometallic material. The Fe_3Ni_7NCMK-3 exhibited the highest conductivity with a value of 2.375×10^{-2} S/m, with the same order of magnitude as Ni_3Zn_7NCMK-3 and Fe_7Ni_3NCMK-3 samples, while the lowest conductivity value is shown by NiNCMK-3 (4.760×10^{-3} S/m). The Fe_3Ni_7NCMK-3 material showed, among the bimetallic materials, a higher surface concentration of Ni and lower concentration of S which could contribute to the high conductivity. High conductivity is important for the transport of electrons and ionic species at the surface and interface favoring efficient diffusion and transport of species to and from the active surface.

Table 2
Surface atomic composition and element concentration determined by XPS using the survey spectra.

Sample	Surface atomic concentration (at.%)							
	C	N	O	Ni	Fe	Zn	S	
NiNCMK-3	84.55	6.45	6.26	1.25	–	–	1.02	–
Fe_3Ni_7NCMK-3	84.66	7.15	6.37	0.69	0.24	–	0.31	Fe:Ni = 0.35
Fe_7Ni_3NCMK-3	81.77	7.39	8.94	0.43	0.30	–	0.48	Fe:Ni = 0.70
Ni_3Zn_7NCMK-3	84.71	7.72	5.65	0.35	–	0.34	0.93	Ni:Zn = 1.1

Table 3
Surface atomic speciation of N and Ni determined by high-resolution XPS spectra.

Sample	Surface speciation (%)										
	N 1 s						Ni 2p				Fe 2p
	pyridinic-N 398.50 ± 0.04 (eV)	Metal-N 399.70 ± 0.23 (eV)	pyrrolic-N 400.71 ± 0.25 (eV)	graphitic-N 402.03 ± 0.57 (eV)	pyridine-N-oxide 403.73 ± 0.46 (eV)	405.52 ± 0.55 (eV)	854.08 (eV)	855.46 ± 0.19 (eV)	856.14 (eV)	857.90 ± 0.38 (eV)	710.90 (eV)
NiNCMK-3	36.80	21.69	33.27	4.83	3.41	–	–	76.8	–	23.2	–
Fe_3Ni_7NCMK-3	32.67	19.43	29.44	7.69	5.05	5.72	–	68.1	19	12.9	N.D.
Fe_7Ni_3NCMK-3	30.63	20.23	25.78	15.37	4.96	3.03	14.8	64.8	–	20.5	100
Ni_3Zn_7NCMK-3	33.57	22.19	29.35	8.65	3.40	2.84	–	100	–	–	–

Table 4
Electronic conductivity values measured for all materials.

Sample	Electronic conductivity (S/m)
NiNCMK-3	4.760×10^{-3}
Fe_3Ni_7NCMK-3	2.375×10^{-2}
Fe_7Ni_3NCMK-3	1.406×10^{-2}
Ni_3Zn_7NCMK-3	1.435×10^{-2}

3.3. Electrocatalytic activity

Fig. 7 shows Faraday Efficiency values for H_2, CO (FE_{H_2} and FE_{CO}, respectively) obtained by gas chromatography from the cathodic compartment in the three compartments electrochemical cell for samples NiNCMK-3, Fe_3Ni_7NCMK-3, Fe_7Ni_3NCMK-3 and Ni_3Zn_7NCMK-3. The current density (*j*) for the cathodic reaction is also included for each sample. High FE_{CO} and FE_{H_2} are observed between potential ranges of 0.8–1.2 V vs. RHE for all electrocatalysts, however most of them show the highest value of *FE* at −1.2 V vs. RHE. Importantly, a reaction performed without catalyst powder and using the gas diffusion electrode with carbon paper without drop-casting of the ink, showed that there is no evolution of CO in the gas phase, evidencing that CO is solely generated by the electrocatalysts. For instance, CO and H_2 evolution depend on the electrocatalyst composition. In addition, CH_4 is not detected, demonstrating the high selectivity of the catalysts to CO and H_2 in the gas phase. Higher activity for CO evolution is observed with

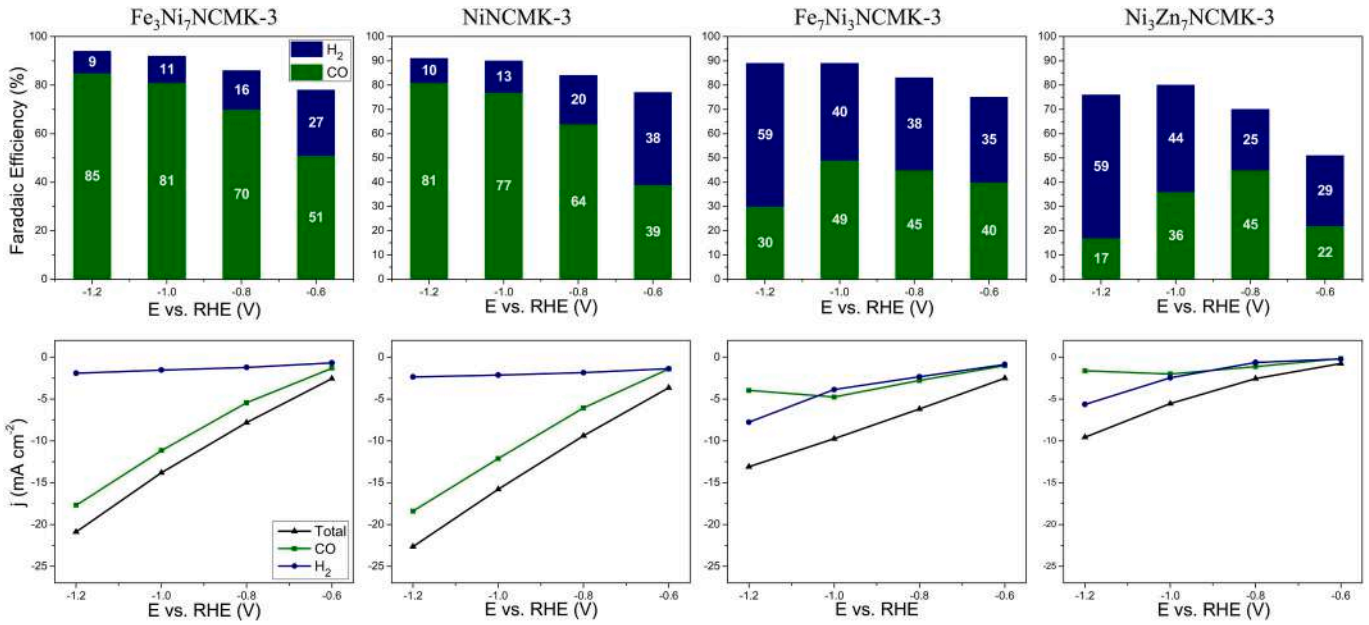

Fig. 7. FE and current density values measured at different potentials vs. RHE (−0.6, −0.8, −1.0 and − 1.2 V) for Fe_3Ni_7NCMK-3, NiNCMK-3, Fe_7Ni_3NCMK-3 and Ni_3Zn_7NCMK-3.

bimetallic electrocatalysts containing Fe and Ni (Fig. 7), while hydrogen evolution, a highly competitive by-product in the electrochemical system, decreases as CO production increases, with Ni_3Zn_7NCMK-3 being most selective to HER. FE_{CO} for Fe_3Ni_7NCMK-3 achieves 85 % at −1.2 V vs. RHE and is the maximum value obtained among the studied electrocatalysts, while NiNCMK-3 achieves 81 % at −1.2 V vs. RHE. On the other hand, Fe_7Ni_3NCMK-3 shows lower FE_{CO} reaching 49 % at −1 V vs. RHE. Regarding current density, j_{total} achieves higher values for samples with higher FE_{CO} i.e., Fe_3Ni_7NCMK-3 and NiNCMK-3 reaching −21 mA cm^{-2} and − 23 mA cm^{-2} at −1.2 V vs. RHE respectively, and partial current densities of CO around −18 mA cm^{-2} and − 34 mA cm^{-2} at −1.2 V vs RHE, which suggest a more selective reaction while Fe_7Ni_3NCMK-3 shows lower j_{total} values, achieving −13 mA cm^{-2} and similar values of partial current densities of CO and H_2. On the other hand, FE and current density values for Ni_3Zn_7NCMK-3 (Fig. 7) show lower values achieving their maximum for FE_{CO} of 45 % at −0.8 V vs. RHE, while for FE_{H_2} it reached 59 % at −1.2 V vs. RHE. The results indicate that Fe_7Ni_3NCMK-3 and Ni_3Zn_7NCMK-3 are more selective to H_2, implying that highly dispersed Zn^{2+} species combined with Ni^{2+} species in a unique chemical environment, can enhance HER with Ni_3Zn_7NCMK-3 catalyst, while the high surface concentration of Fe^{3+} species in Fe_7Ni_3NCMK-3 catalyst also favors HER. For comparison, to analyse the impact of the material composition in the electrocatalytic activity, a material containing cobalt was prepared, Fe_3Co_7NCMK-3 (Fig. S2). The results evidenced that this material exhibits the lowest conductivity among the set of studied materials, reaching 4.050×10^{-3} S/m. It also showed low efficiency in the electrocatalytic reduction of CO_2 to CO reaching a *FE* for CO of 22 % at −0.8 V vs. RHE, with a current density of −7 mA cm^{-2} at 1.2 V vs. RHE, indicating higher selectivity to H_2 evolution reaction (Fig. S2). The composition of SACs electrocatalysts plays a key role in activity and selectivity. Nickel species combined with iron species on an N-doped carbonaceous support, with a surface atomic concentration of nickel species three times higher than that of iron, and with a surface enriched in Ni^{2+} species in different chemical environments in Fe_3Ni_7NCMK-3 are responsible for high FE to CO. Remarkable, high FE_{CO} can also be achieved at lower potentials reaching 70 % at −0.8 V vs. RHE (Fig. 7a), with a total current density of −7.0 mA cm^{-2}. It is important to highlight that compared to NiNCMK-3, the Fe_3Ni_7NCMK-3 electrocatalyst shows higher FE_{CO} at low potentials (Fig. 7).

Fig. 8 shows production rate values for H_2 and CO, reported per S_{BET} of the catalysts and per site of the main species of Ni^{2+} determined by XPS at 855.46 ± 0.19 eV (Table 3), obtained by the same gas chromatography test done for obtaining FE values. As for FE values, higher production rate values for CO are observed between potential ranges of −0.8–1.2 V vs. RHE for both Fe_3Ni_7NCMK-3 and NiNCMK-3 electrocatalysts, more specifically, the higher the potential applied the higher the production of CO and H_2, however, as the applied potential increases, the increase in CO production is exponentially higher than the increase in H_2 production and hence the molar ratio between the two products is changing, increasing the potential. These results justify the FE values observed with increasing applied potential for both catalysts. The molar ratio CO/H_2 obtained on Fe_3Ni_7NCMK-3 was from 2:1 at −0.6 V vs. RHE to 9:1 at −1.2 V vs. RHE, with the higher CO production rate of 6.85×10^{-1} μmol CO s^{-1} m^{-2} per Ni^{2+} at the surface at that potential, while the molar ratio CO/H_2 obtained on NiNCMK-3 was from 1:1 at −0.6 V vs. RHE to 8:1 at −1.2 V vs. RHE, with the higher CO production rate of 4.57×10^{-1} μmol CO s^{-1} m^{-2} per Ni^{2+} at the surface at that potential. From these molar production ratios, it can also be seen that Fe_3Ni_7NCMK-3 is more selective for CO production in the CO_2 reduction reaction.

Table 5 presents a summary of results in literature with Ni or Ni + Fe species dispersed on carbonaceous materials. The Faradaic efficiency to CO obtained with Fe_3Ni_7NCMK-3 electrocatalyst is in line with other reported materials. Compared to previously reported catalysts, Fe_3Ni_7NCMK-3 catalyst demonstrates a uniquely broad tunability in the CO/H_2 ratio, ranging from 2:1 to 9:1, while maintaining a high Faradaic efficiency for CO (FE_{CO} = 85 %). This performance is superior to most systems listed, which either do not report syngas ratios or show limited control over gas product distribution. Notably, our catalyst achieves this performance in 1 M $KHCO_3$ electrolyte, offering a more concentrated and industrially relevant medium compared to the 0.5 M systems typically used. Together, these results underscore the versatility and application potential of our system for targeted syngas production.

Table 5
Comparison of the catalytic performance of various reported materials with Ni or Ni + Fe in literature with those prepared in this work.

Material	Electrolyte	FE_{CO} (%)	CO/H_2 ratio	Reference
TAP 900@Fe	0.5 M $KHCO_3$	93.5 ± 3.7	–	[10]
TAP 900@Ni	0.5 M $KHCO_3$	95.3 ± 4.7	–	
A-Ni-NSNG	0.5 M $KHCO_3$	97	–	[28]
Ni-N-C	0.5 M $KHCO_3$	97	–	[19]
Ni-N_3C_1	0.5 M $KHCO_3$	71.9	–	[2]
2 mM-Ni,N-C-800	0.1 M $KHCO_3$	94.8	–	[29]
0.1 Ni@NCNT-C-800	0.5 M $KHCO_3$	90	–	[30]
Ni-N-hCNCs	0.5 M $KHCO_3$	94 %	suppressed HER	[48]
Ni-SN-hCNCs	0.5 M $KHCO_3$	95 %		
Ni/N-C-100	0.5 M $KHCO_3$	91.1 %	suppressed HER	[49]
NiNCMK-3	1 M $KHCO_3$	81	1:1–8:1	This work
Fe_2Ni/NG	0.5 M $KHCO_3$	60.9	1.2–2.9	[31]
Fe_3Ni_7-NC	0.5 M $KHCO_3$	81.3	1:1–6:1	[23]
Fe_3Ni_7NCMK-3	1 M $KHCO_3$	85	2:1–9:1	This work

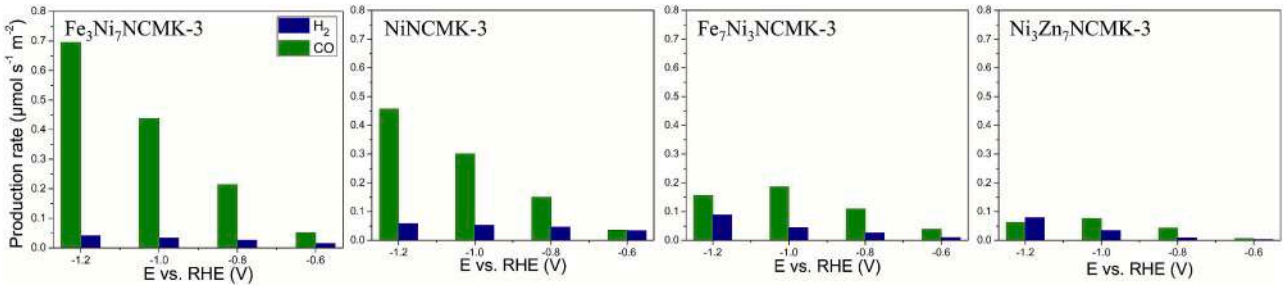

Fig. 8. Production rate values measured at different potentials vs. RHE (−0.6, −0.8, −1.0 and − 1.2 V) for Fe_3Ni_7NCMK-3, NiNCMK-3, Fe_7Ni_3NCMK-3 and b) Ni_3Zn_7NCMK-3.

The better electrocatalytic activity of Fe_3Ni_7NCMK-3 material could be attributed to: i) the high dispersion of Ni and Fe, as observed with STEM-EDX, HRTEM and HAADF, allowing high atomic efficiency and selectivity; ii) the high surface area and pore volume with an ordered porous structure allowing better access of CO_2 to the active sites, as it has been reported that nanoconfinement of active species might favor interaction of the reagent molecules with active sites in electrochemistry allowing proper activation and redox reactions [47], in addition the ordered pore structure with uniform mesopores might also accelerate electrolyte penetration and diffusion of CO_2 to active sites and CO diffusion from the catalyst surface [48]; and iii) among the bimetallic materials, it showed the highest surface concentration of Ni^{2+} species in different chemical environments, and lower concentration of S, which could enhance adsorption and activation of CO_2 to CO. The reaction rate determined by considering the S_{BET} and surface concentration of Ni^{2+} on the surface reached 6.85×10^{-1} μmol CO s^{-1} m^{-2} per Ni^{2+} at the surface while with NiNCMK-3 reached 4.57×10^{-1} μmol CO s^{-1} m^{-2} per Ni^{2+} at the surface (6.23×10^{-2} and 1.55×10^{-1} for Ni_3Zn_7NCMK-3 and Fe_7Ni_3NCMK-3 respectively).

N-doped carbonaceous materials have been reported to induce polarization of C atoms, enhancing electronic density on N and thus promoting electronic and ionic conductivity [11]; the electron pair in pyridinic-N has been identified as anchoring site for adsorbing and activating CO_2 [24], while graphitic-N has also been reported as contributing in lowering the energy barrier [11,24]. The XPS characterization of N 1 s (Fig. 6, Tables 2 and 3) shows that all materials in our work exhibit similar surface concentration of N and pyridinic-N, but conductivity and electrochemical activity in ECO_2RR varied with the composition of transition metals. For instance, all materials were able to adsorb and activate CO_2, but the transition metals played a key function in the ECO_2RR activity and selectivity. NiNCMK-3 and Fe_3Ni_7NCMK-3 showed the higher activities and selectivities to CO (Fig. 5), with Fe_3Ni_7NCMK-3 exhibiting better catalytic performance. In ECO_2RR to CO, *COOH must be strongly adsorbed while *CO must be rapidly desorbed from the surface to achieve high selectivity and production rate of CO [14]. Likely the high surface concentration of Ni^{2+} on the surface of Fe_3Ni_7NCMK-3 electrocatalyst in different chemical environments, combined with Fe^{3+} species on the surface, increased adsorption and activation of CO_2 through *COOH while favoring a rapid desorption of CO. Theoretical studies on graphene and N-doped graphene have demonstrated that defect sites favor adsorption and activation of CO_2 through the *COOH intermediate while they do not favor

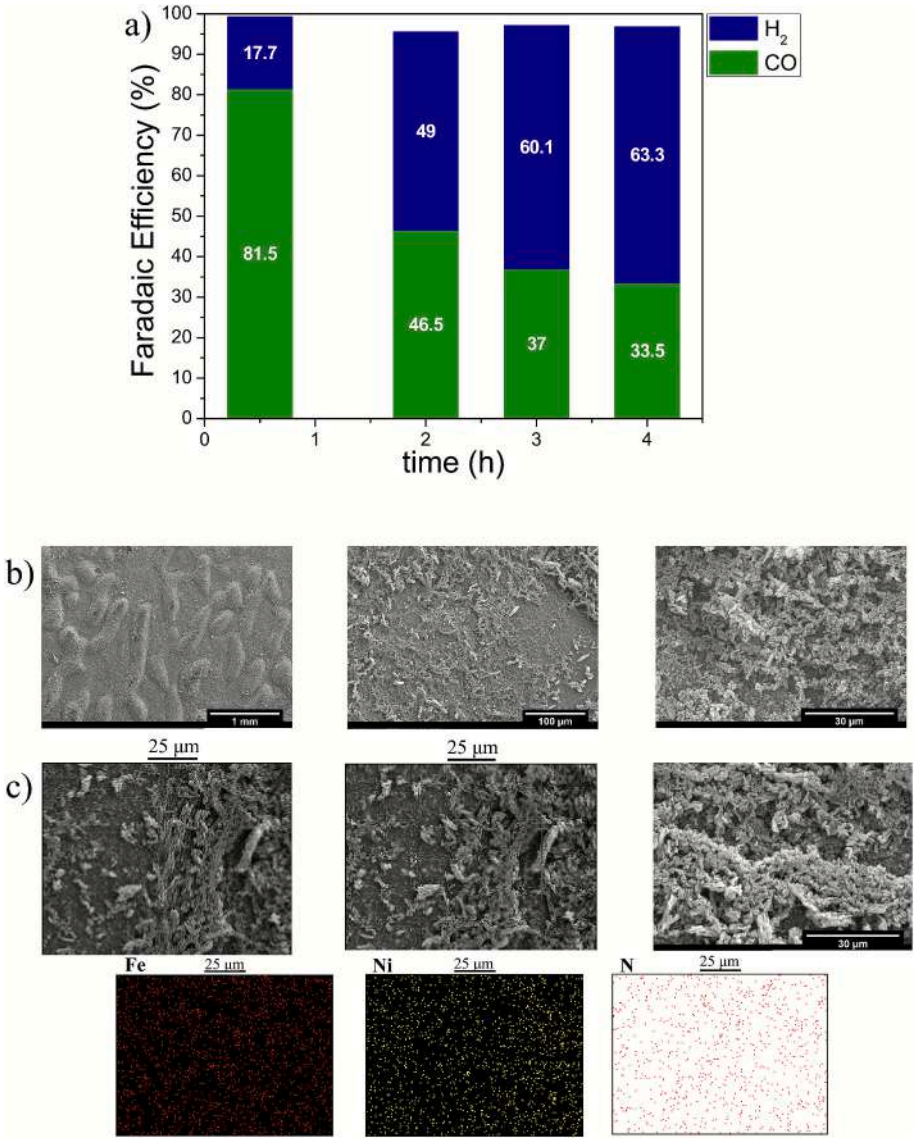

Fig. 9. Stability test with Fe_7Ni_3NCMK-3 electrocatalyst: a) evolution of FE to CO and H_2 measured at −1.0 V vs RHE over time, b) SEM micrographs of the electrode with Fe_7Ni_3NCMK-3 before test, c) SEM-EDS characterization of the electrode with spent Fe_7Ni_3NCMK-3 electrocatalyst.

that of CO which is rapidly desorbed [25], consequently the introduction of nitrogen, nickel and iron in Fe_3Ni_7NCMK-3 electrocatalyst with regard to nitrogen and nickel in NiNCMK-3 indicates a major number of defects in Fe_3Ni_7NCMK-3 favoring ECO2RR and low activity to HER.

3.4. Stability test

The activity of Fe_3Ni_7NCMK-3 electrocatalyst is evaluated over time, using a fresh prepared electrode, at a selected potential of −1.0 V vs. RHE (Fig. 9a). The results evidenced that after 30 min reaction the FE to CO reached 81.5 % and total current density reached −11.2 mA cm^{-2}, values that are comparable to those obtained with the first measure at 81 % and − 14 mA cm^{-2} respectively (Fig. 7), indicating the results are repeatable and the homogeneous nature of the catalyst and electrode preparation. Importantly, in the gas phase only CO and H_2 were generated without formation of CH_4, indicating the electrocatalyst remained highly selective to CO and H_2 production in gas phase. Nevertheless, after 0.5 h of operation the FE to CO decreased while FE to H_2 increased suggesting a change in activity of the electrocatalyst rather than a deactivation, reaching after 4 h reaction FE_{CO} and FE_{H_2} of 34 % and 63 % respectively, while total current density after 2 h reaction remains at −9.4 ± 0.3 mA cm^{-2}. After 4 h of continuous operation, excessive wetting of the electrode led to catholyte permeation into the gas chamber of the cell compromising the operation and gas flow, factors that can also contribute to gradual decline in catalytic performance. For safety reasons, in particular with CO generation, gas chromatography measurements were halted after 4 h, although electrochemical operation continued for a total of 48 h be monitored. On the other hand, the pH did not change and was maintained in the 8–9 range. The electrode with Fe_3Ni_7NCMK3 electrocatalyst before test was characterized using SEM (Fig. 9b), the micrographs show homogeneous distribution of the Fe_3Ni_7NCMK3 particles. Postmortem characterization of the electrode using SEM-EDS after 48 h under electrochemical operation shows the Fe_3Ni_7NCMK3 particles remained on the electrode surface (Fig. 9c), while EDS analysis shows that nickel, iron and even nitrogen species remained rather homogenously distributed in the catalyst and electrode. For instance, the decrease in CO selectivity must be attributed to chemical changes on the surface. Further characterization of the postmortem electrocatalyst and electrode is needed for a deeper understanding of the physicochemical properties changes during operation which could lead to improve stability.

4. Conclusions

In this work we demonstrated that phenanthroline complexes of Ni + Fe, Ni + Zn combined with nanoreplication of SBA-15 hard template led to the formation of porous carbonaceous materials simultaneously dispersing N, Ni + Fe and N, Ni + Zn; with atomic dispersion of Ni, Fe, Zn species. The N-doped porous carbonaceous materials containing Ni, Ni + Fe or Ni + Zn species showed an ordered mesopore structure with high surface area and pore volume. The composition and the molar ratio between the metals, in particular with higher surface atomic concentration of Ni than Fe or Zn, influenced the surface atomic composition, with Fe_3Ni_7NCMK-3 materials showing the higher surface concentration of Ni, mainly in the Ni^{2+} oxidation state in different chemical environments. The conductivity and activity in the electrocatalytic CO_2 reduction to CO were dependent on the material composition, the Fe_3Ni_7NCMK-3 material showed the highest Faradaic efficiency reaching 85 % at −1.2 V vs. RHE, and importantly it also showed high Faradaic efficiency of 70 % at −0.8 V vs. RHE. For instance, the composition and the molar ratio between the metals, in particular with higher surface atomic concentration of Ni than Fe or Zn, influenced activity in ECO_2RR to CO. The surface enrichment in Ni^{2+} species, especially in low coordinated Ni^{2+} species, played a key role in the selective conversion of CO_2 to CO, with high reaction rate of 6.85×10^{-1} μmol CO s^{-1} m^{-2} per Ni^{2+} at the surface. These materials improve the efficiency of this reaction offering a more viable and economical alternative to traditional catalysts and providing a product of high added value for its versatile and necessary use in an energy industry focused on a more sustainable future.

CRediT authorship contribution statement

Ruben Palacio: Writing – review & editing, Writing – original draft, Validation, Supervision, Investigation, Formal analysis, Conceptualization. **Daniela Jaramillo:** Writing – review & editing, Writing – original draft, Validation, Methodology, Investigation, Formal analysis. **Elías Rodríguez-Jara:** Writing – review & editing, Writing – original draft, Validation, Investigation, Formal analysis. **Ryosuke Nakazato:** Writing – review & editing, Writing – original draft, Validation, Methodology, Investigation, Formal analysis. **Matthias Quintelier:** Writing – review & editing, Writing – original draft, Validation, Methodology, Investigation, Formal analysis. **Keeko Matsumoto:** Writing – review & editing, Writing – original draft, Validation, Methodology, Investigation, Formal analysis. **Joke Hadermann:** Writing – review & editing, Writing – original draft, Supervision, Project administration, Funding acquisition, Formal analysis. **Kiyoharu Tadanaga:** Writing – review & editing, Writing – original draft, Supervision, Project administration, Funding acquisition, Formal analysis. **Nataly Carolina Rosero-Navarro:** Writing – review & editing, Writing – original draft, Validation, Supervision, Project administration, Funding acquisition, Formal analysis, Conceptualization.

Author contributions

The manuscript was written through contributions of all authors. All authors have given approval to the final version of the manuscript.

Declaration of competing interest

The authors declare that they have no known competing financial interests or personal relationships that could have appeared to influence the work reported in this paper.

Acknowledgements

This research was supported through 4AirCRAFT project under the strategic international cooperation between Europe (Horizon2020, No.101022633) and Japan Science and Technology Agency (JST) with reference number JPMJSC2102. N.C. R-N. acknowledge the financial support through the Ramón y Cajal grant No. RYC2020–029909-I of the Spanish State Research Agency, the IDEAL-Li Project (Ref. PIE - 2022AT009, Talent Attraction) of The Spanish National Research Council (CSIC) and the FPU contract No. FPU22/03909 of the Spanish Ministry of Science, Innovation and Universities. The authors also thank to the University of Antioquia UdeA. UdeA-ICV collaboration by COOPB23103 project from CSIC International projects.

Appendix A. Supplementary data

Supplementary data to this article can be found online at https://doi.org/10.1016/j.cej.2025.172327.

Data availability

Data will be made available on request.

References

[1] IPCC, Sections, in: Core Writing Team, H. Lee, J. Romero (Eds.), Climate Change 2023: Synthesis Report. Contribution of Working Groups I, II and III to the Sixth Assessment Report of the Intergovernmental Panel on Climate Change, IPCC,

Geneva, Switzerland, 2023, pp. 35–115, https://doi.org/10.59327/IPCC/AR6-9789291691647.
[2] J. Han, X. Bai, X. Xu, X. Bai, A. Husile, S. Zhang, L. Qi, J. Guan, Advances and challenges in the electrochemical reduction of carbon dioxide, Chem. Sci. 15 (2024) 7870–7907.
[3] C.E.i. IEA, IEA, Paris https://www.iea.org/reports/co2-emissions-in-2023, Licence: CC BY 4 (0) (2024).
[4] Y.Y. Birdja, E. Pérez-Gallent, M.C. Figueiredo, A.J. Göttle, F. Calle-Vallejo, M.T. M. Koper, Advances and challenges in understanding the electrocatalytic conversion of carbon dioxide to fuels, Nat. Energy 4 (2019) 732–745.
[5] D. Gao, R.M. Arán-Ais, H.S. Jeon, B. Roldan Cuenya, Rational catalyst and electrolyte design for CO_2 electroreduction towards multicarbon products, Nat. Catal. 2 (2019) 198–210.
[6] Y. Hua, J. Wang, T. Min, Z. Gao, Electrochemical CO_2 conversion towards syngas: Recent catalysts and improving strategies for ratio-tunable syngas, J. Power Sources 535 (2022) 231453.
[7] P. Preikschas, J. Zhang, R.R. Seemakurthi, Z. Lian, A.J. Martín, S. Xi, F. Krumeich, H. Ma, Y. Zhou, N. López, B.S. Yeo, J. Pérez-Ramírez, CO_2 Electroreduction to Long-Chain Hydrocarbons on Cobalt Catalysts, Adv. Energy Mater. 14 (2024) 2401447.
[8] S. Liang, L. Huang, Y. Gao, Q. Wang, B. Liu, Electrochemical Reduction of CO_2 to CO over Transition Metal/N-Doped Carbon Catalysts: The Active Sites and Reaction Mechanism, Adv. Sci. 8 (2021) 2102886.
[9] J.H. Lee, S. Kattel, Z. Jiang, Z. Xie, S. Yao, B.M. Tackett, W. Xu, N.S. Marinkovic, J. G. Chen, Tuning the activity and selectivity of electroreduction of CO_2 to synthesis gas using bimetallic catalysts, Nat. Commun. 10 (2019) 3724.
[10] S.C. Sarma, J. Barrio, A. Bagger, A. Pedersen, M. Gong, H. Luo, M. Wang, S. Favero, C.X. Zhao, Q. Zhang, A. Kucernak, M.M. Titirici, I.E.L. Stephens, Reaching the Fundamental Limitation in CO_2 Reduction to CO with Single Atom Catalysts, Adv. Funct. Mater. 33 (2023) 2302468.
[11] T. Zheng, K. Jiang, H. Wang, Recent Advances in Electrochemical CO_2-to-CO Conversion on Heterogeneous Catalysts, Adv. Mater. 30 (2018) 1802066.
[12] B. Chang, Z. Min, N. Liu, N. Wang, M. Fan, J. Fan, J. Wang, Electrocatalytic CO_2 reduction to syngas, Green, Energy Environ. 9 (2024) 1085–1100.
[13] C. Wang, X. Wang, H. Ren, Y. Zhang, X. Zhou, J. Wang, Q. Guan, Y. Liu, W. Li, Combining Fe nanoparticles and pyrrole-type Fe-N_4 sites on less-oxygenated carbon supports for electrochemical CO_2 reduction, Nat. Commun. 14 (2023) 5108.
[14] K. Jiang, S. Siahrostami, T. Zheng, Y. Hu, S. Hwang, E. Stavitski, Y. Peng, J. Dynes, M. Gangisetty, D. Su, K. Attenkofer, H. Wang, Isolated Ni single atoms in graphene nanosheets for high-performance CO_2 reduction, Energy Environ. Sci. 11 (2018) 893–903.
[15] H. Jiao, C. Wang, H. Tian, Z.-Y. Zhang, Y. Zhao, P. Na, Y. Yamauchi, Z.-L. Wang, Strong interaction heterointerface of NiFe oxyhydroxide/cerium oxide for efficient and stable water oxidation, Chem. Eng. J. 498 (2024) 155063.
[16] H. Tian, J.-T. Yang, X. Wang, H. Jiao, Z.-F. Gao, K.-Y. Zhu, Q. He, Z.-L. Wang, Ionic liquid-TiO_2-CuOx composite interfaces combined with gas directional transmission for enhanced electrooxidation of methane to ethanol, Appl. Catal. B Environ. Energy 375 (2025) 125411.
[17] L. Bian, Y. Bai, J.-Y. Chen, H.-K. Guo, S. Liu, H. Tian, N. Tian, Z.-L. Wang, Hierarchical Tandem Catalysis Promotes CO Spillover and Trapping for Efficient CO_2 Reduction to C_{2+} Products, ACS Nano 19 (2025) 9304–9316.
[18] Y. Cheng, S. Zhao, B. Johannessen, J.P. Veder, M. Saunders, M.R. Rowles, M. Cheng, C. Liu, M.F. Chisholm, R. De Marco, H.M. Cheng, S.Z. Yang, S.P. Jiang, Atomically Dispersed Transition Metals on Carbon Nanotubes with Ultrahigh Loading for Selective Electrochemical Carbon Dioxide Reduction, Adv. Mater. 30 (2018) e1706287.
[19] J. Wang, Y.-C. Huang, Y. Wang, H. Deng, Y. Shi, D. Wei, M. Li, C.-L. Dong, H. Jin, S. S. Mao, S. Shen, Atomically Dispersed Metal–Nitrogen–Carbon Catalysts with d-Orbital Electronic Configuration-Dependent Selectivity for Electrochemical CO_2-to-CO Reduction, ACS Catal. 13 (2023) 2374–2385.
[20] Y.-M. Wang, F.-Q. Yan, Q.-Y. Wang, C.-X. Du, L.-Y. Wang, B. Li, S. Wang, S.-Q. Zang, Single-atom tailored atomically-precise nanoclusters for enhanced electrochemical reduction of CO_2-to-CO activity, Nat. Commun. 15 (2024) 1843.
[21] A.U. Rehman, T. Zhao, S. Yun, K. Dou, W. Zhu, F. Zhang, Precise Synthesis of Single-Atom Catalysts for Boosting Next-Generation Advanced Oxidation and Reduction Processes in Sustainable Energy Applications, ChemCatChem 17 (2024) e202401186.
[22] H. Yang, L. Shang, Q. Zhang, R. Shi, G.I.N. Waterhouse, L. Gu, T. Zhang, A universal ligand mediated method for large scale synthesis of transition metal single atom catalysts, Nat. Commun. 10 (2019) 4585.
[23] X. Han, Y. Chang, T. Yue, M. Jia, J. Jia, Fe-Ni bimetallic composite N-doped carbon catalyst for electrocatalytic reduction of CO_2 to produce efficient and controlled syngas, J. Alloys Compd. 971 (2024) 172772.
[24] P.P. Sharma, J. Wu, R.M. Yadav, M. Liu, C.J. Wright, C.S. Tiwary, B.I. Yakobson, J. Lou, P.M. Ajayan, X.-D. Zhou, Nitrogen-Doped Carbon Nanotube Arrays for High-Efficiency Electrochemical Reduction of CO_2: On the Understanding of Defects, Defect Density, and Selectivity, Angew. Chem. Int. Ed. 54 (2015) 13701–13705.
[25] S. Siahrostami, K. Jiang, M. Karamad, K. Chan, H. Wang, J. Nørskov, Theoretical Investigations into Defected Graphene for Electrochemical Reduction of CO_2, ACS Sustain. Chem. Eng. 5 (2017) 11080–11085.
[26] J. Yin, J. Jin, Z. Yin, L. Zhu, X. Du, Y. Peng, P. Xi, C.-H. Yan, S. Sun, The built-in electric field across FeN/Fe_3N interface for efficient electrochemical reduction of CO_2 to CO, Nat. Commun. 14 (2023) 1724.
[27] C. Zhao, X. Dai, T. Yao, W. Chen, X. Wang, J. Wang, J. Yang, S. Wei, Y. Wu, Y. Li, Ionic Exchange of Metal-Organic Frameworks to Access Single Nickel Sites for Efficient Electroreduction of CO_2, J. Am. Chem. Soc. 139 (2017) 8078–8081.
[28] H.B. Yang, S.-F. Hung, S. Liu, K. Yuan, S. Miao, L. Zhang, X. Huang, H.-Y. Wang, W. Cai, R. Chen, J. Gao, X. Yang, W. Chen, Y. Huang, H.M. Chen, C.M. Li, T. Zhang, B. Liu, Atomically dispersed Ni(i) as the active site for electrochemical CO_2 reduction, Nat. Energy 3 (2018) 140–147.
[29] X. Tan, C. Yu, S. Cui, L. Ni, W. Guo, Z. Wang, J. Chang, Y. Ren, J. Yu, H. Huang, J. Qiu, Activity descriptor of Ni,N-Codoped carbon electrocatalyst in CO_2 electroreduction reaction, Chem. Eng. J. 433 (2022) 131965.
[30] M. Liang, Y. Liu, H. Huang, L. Diao, J. Mu, Z. Miao, J. Zhou, S. Zhuo, A robust Ni@NCNT-C catalyst for highly efficient electrochemical CO_2 reduction to CO over a wide potential range, Chem. Eng. J. 450 (2022) 137962.
[31] T. Yue, Y. Chang, J. Liu, J. Jia, M. Jia, Fe−Ni Nanoparticles on N-doped Carbon as Catalysts for Electrocatalytic Reduction of CO_2 to Tune CO/H_2 Ratio, ChemElectroChem 8 (2021) 4233–4239.
[32] J.J. Bolívar Caballero, I.N. Zaini, W. Yang, Reforming processes for syngas production: A mini-review on the current status, challenges, and prospects for biomass conversion to fuels, Appl. Energ. Combust. Sci. 10 (2022) 100064.
[33] R. Bates, K. Dölle, Syngas Use in Internal Combustion Engines - A Review, Adv. Dent. Res. 10 (2017) 1–8.
[34] D. Jaramillo, G. Alvarez, C. Díaz, S. Pérez, J. Muñoz Saldaña, L. Sierra, B.L. López, A. Moreno-Zuria, M. Mohamedi, R. Palacio, Porous carbonaceous materials simultaneously dispersing N, Fe and Co as bifunctional catalysts for the ORR and OER: electrochemical performance in a prototype of a Zn–air battery, Dalton Trans. 53 (2024) 3143–3158.
[35] R. Palacio, J. Gallego, Z. Gabelica, C. Batiot-Dupeyrat, J. Barrault, S. Valange, Decomposition of ethanol into H_2-rich gas and carbon nanotubes over Ni, Co and Fe supported on SBA-15 and Aerosil, Appl. Catal. A Gen. 504 (2015) 642–653.
[36] H. Zhong, Y. Su, R. Ma, Y. Luo, H. Lin, J. Gu, Z. Gong, Y. Yang, Nano-Scale Interface Engineering of Sulfur Cathode to Enable High-Performance All-Solid-State Li–S Batteries, Adv. Funct. Mater. 34 (2024) 2315925.
[37] R. Nakazato, K. Matsumoto, N. Yamaguchi, M. Cavallo, V. CrocellÀ, F. Bonino, M. Quintelier, J. Hadermann, N.C. Rosero-Navarro, A. Miura, K. Tadanaga, CO_2 Electrochemical Reduction with Zn-Al Layered Double Hydroxide-Loaded Gas-Diffusion Electrode, Electrochemistry 91 (2023) 097003.
[38] X. Wu, J.W. Sun, P.F. Liu, J.Y. Zhao, Y. Liu, L. Guo, S. Dai, H.G. Yang, H. Zhao, Molecularly Dispersed Cobalt Phthalocyanine Mediates Selective and Durable CO_2 Reduction in a Membrane Flow Cell, Adv. Funct. Mater. 32 (2022) 2107301.
[39] M. Thommes, K. Kaneko, V. Neimark Alexander, P. Olivier James, F. Rodriguez-Reinoso, J. Rouquerol, S.W. Sing Kenneth, Physisorption of gases, with special reference to the evaluation of surface area and pore size distribution (IUPAC Technical Report), Pure Appl. Chem. (2015) 1051.
[40] M. Ayiania, M. Smith, A.J.R. Hensley, L. Scudiero, J.-S. McEwen, M. Garcia-Perez, Deconvoluting the XPS spectra for nitrogen-doped chars: An analysis from first principles, Carbon 162 (2020) 528–544.
[41] D. Guo, R. Shibuya, C. Akiba, S. Saji, T. Kondo, J. Nakamura, Active sites of nitrogen-doped carbon materials for oxygen reduction reaction clarified using model catalysts, Science 351 (2016) 361.
[42] J. Zhang, Z. Zhao, Z. Xia, L. Dai, A metal-free bifunctional electrocatalyst for oxygen reduction and oxygen evolution reactions, Nat. Nanotechnol. 10 (2015) 444–452.
[43] M.C. Biesinger, B.P. Payne, A.P. Grosvenor, L.W.M. Lau, A.R. Gerson, R.S.C. Smart, Resolving surface chemical states in XPS analysis of first row transition metals, oxides and hydroxides: Cr, Mn, Fe, Co and Ni, Appl. Surf. Sci. 257 (2011) 2717–2730.
[44] M.C. Biesinger, B.P. Payne, L.W.M. Lau, A. Gerson, R.S.C. Smart, X-ray photoelectron spectroscopic chemical state quantification of mixed nickel metal, oxide and hydroxide systems, Surf. Interface Anal. 41 (2009) 324–332.
[45] M.C. Biesinger, L.W.M. Lau, A.R. Gerson, R.S.C. Smart, The role of the Auger parameter in XPS studies of nickel metal, halides and oxides, Phys. Chem. Chem. Phys. 14 (2012) 2434–2442.
[46] A.M. Mohammed, S.S. Mohtar, F. Aziz, M. Aziz, A. Ul-Hamid, Cu_2O/ZnO-PANI ternary nanocomposite as an efficient photocatalyst for the photodegradation of Congo Red dye, J. Environ. Chem. Eng. 9 (2021) 105065.
[47] J. Wordsworth, T.M. Benedetti, S.V. Somerville, W. Schuhmann, R.D. Tilley, J. J. Gooding, The Influence of Nanoconfinement on Electrocatalysis, Angew. Chem. Int. Ed. 61 (2022) e202200755.
[48] Y. Chen, Y. Yao, Y. Xia, K. Mao, G. Tang, Q. Wu, L. Yang, X. Wang, X. Sun, Z. Hu, Advanced Ni-Nx-C single-site catalysts for CO_2 electroreduction to CO based on hierarchical carbon nanocages and S-doping, Nano Res. 13 (2020) 2777–2783.
[49] S.-J. Zheng, H. Cheng, J. Yu, Q. Bie, J.-D. Chen, F. Wang, R. Wu, D.J. Blackwood, J.-S. Chen, Three-dimensional ordered porous N-doped carbon-supported accessible Ni-Nx active sites for efficient CO_2 electroreduction, Rare Metals 42 (2023) 1800–1807.